Finite volume simulation of photothermal microscopy for detecting closely spaced subsurface defects in optical materials

Ivan Babushkin[1,2,3], Shijie Liu(刘世杰)[1,3,†], and Jianda Shao(郡建达)[1,3]

1 Optical Testing and Characterization Center, Department of High-power Laser Optics Technology and Engineering, Shanghai Institute of Optics and Fine Mechanics, Chinese Academy of Sciences, Shanghai 201815, China

2 University of Chinese Academy of Sciences, Beijing 100049, China

3 China-Russian Belt and Road Joint Laboratory on Laser Science, Shanghai Institute of Optics and Fine Mechanics, Chinese Academy of Sciences, Shanghai, China

†Corresponding author. E-mail: shijieliu@siom.ac.cn

Abstract A frequency domain finite volume model is developed to describe photothermal microscopy of subsurface absorbing defects in optical substrates and to predict how the measurable signals depend on experimental and material parameters. The harmonic heat conduction equation is solved on an adaptive non uniform three-dimensional grid; pump laser heating is represented by a Gaussian intensity profile with Beer–Lambert absorption, and the absorption of gold particles is estimated from Mie theory. The complex temperature field is integrated along the optical axis and weighted by the probe beam intensity profile to yield amplitude and phase observables. The simulated amplitude and phase trends versus defect depth and modulation frequency reproduce the expected diffusion-limited behavior, supporting the physical consistency of the approach for modeling photothermal microscopy. Parameter maps identify the combinations of pump and probe focus positions and beam waists that maximize detectability, and two particle simulations reveal thermal-overlap effects that make closely spaced defects difficult to resolve. The model provides quantitative relationships between modulation frequency, focus depth, and beam size for selecting experimental conditions, supports calibration samples with embedded gold particles, and enables interpretation of measured signals from clustered or arbitrarily shaped defects. An analytical harmonic point-source result agrees with the finite-volume peak temperature amplitudes within 2.6%.

Keywords: photothermal microscopy, finite volume method, subsurface defects, frequency domain simulation

PACS: 44.10.+i, 78.20.nb, 02.70.-c, 81.70.Cv

1. Introduction

Defects introduced during the processing of optical components (cutting, grinding, polishing, cleaning) include cracks, scratches and embedded contaminant particles. Such defects are commonly classified into surface and subsurface defects. Surface defects appear as concave or convex topographies and can be characterized using profilometry or atomic force microscopy, whereas subsurface defects can be more effectively detected using photothermal microscopy (PTM). Localized optical absorption at subsurface defects can produce elevated local temperatures, accelerate material degradation, and lead to failure under high fluence [1].

PTM is a non-destructive technique which can be used for analysis of defects in optical materials by measuring thermally induced perturbations of an optical probe laser field. PTM typically employs a modulated heating (pump) laser whose absorption by a metal particle or an absorbing inclusion generates heat that diffuses into the host medium. The resulting local temperature gradient produces a refractive index gradient (a "thermal lens") around the heated region, which perturbs a probe beam; the perturbed probe signal is detected and demodulated with a lock-in amplifier [2]. Recent papers include lateral resolution enhancement using oppositely phased Gaussian and Laguerre–Gaussian heating beams [3], and photothermal common-path interferometry for assessing weakly absorbing defects on fused silica surfaces and their correlation with laser induced damage [4].

Key experimental parameters for PTM, such as beam waists, modulation frequencies, and relevant sample geometries and material properties, are summarized in a review article and experimental studies [1,2,5]. The dependence of photothermal detection sensitivity on probe beam wavelength, waist position, and detection distance has been analyzed in surface thermal lens and photothermal deflection studies [5,6]. A comprehensive analytical toolbox has been introduced for modeling frequency domain photothermal signals in multilayered structures, providing a master equation for thermal impedance based on one-dimensional heat diffusion [7]. Also, a predictive numerical model has been proposed for photothermal phase signals from absorbing particles of arbitrary size and geometry [8] and time-harmonic thermal interactions in plasmonic particle systems were established [9].

This work combines, within one three-dimensional finite-volume model, finite-size subsurface absorbers whose dimensions are comparable to the pump beam radius, spatially varying pump beam excitation and Beer–Lambert attenuation, heterogeneous particle/host thermal properties, a complex reflective response, and lateral scans of two closely spaced particles to examine thermal overlap and resolution loss. The contribution is thus the integrated numerical treatment and its application to depth, focus, frequency, and clustered-defect signal analyses. The remainder of the paper is organized as follows: Section 2 presents the theoretical model and its finite volume discretization, Section 3 describes the simulations and discusses the results, and Section 4 summarizes the main conclusions.

2. Theoretical model

We model heat conduction in solid media with volumetric heating. In the time domain the temperature field T(r,t) satisfies [10]

$$\rho(r)c(r)\frac{\partial T(r,t)}{\partial t} = \nabla \cdot (k(r)\nabla T(r,t)) + Q(r,t) \quad (1)$$

where ρ(r) is the density (kg m^{-3}), c(r) is the specific heat (J kg^{-1} K^{-1}), k(r) is the thermal conductivity (W m^{-1} K^{-1}), and Q (r,t) is the volumetric heating rate (W m^{-3}).

For a harmonic pump laser modulated at angular frequency ω, we solve in the frequency domain for the complex amplitude T(r), assuming a time dependence exp(iωt) [10]:

$$-\nabla \cdot (k(r)\nabla T(r)) + i\omega\rho(r)c(r)T(r) = Q(r) \quad (2)$$

The substrate is shaped as a parallelepiped. The boundary conditions are as follows: on the top surface (Z = 0), we include convective heat transfer [10]:

$$-k\frac{\partial T}{\partial n}|_{top} = h_{top}T \quad (3)$$

where h_{top} is the convective heat transfer coefficient (W m^{-2} K^{-1}).

In the finite volume discretization, the convective condition on a boundary face of area A_{face} and cell volume V_p contributes a diagonal matrix term $h_{top}A_{face}/V_p$ and a right-hand-side term $h_{top}A_{face}T_\infty/V_p$.

All other external boundaries are thermally insulated and satisfy zero normal heat flux.

We partition the domain into hexahedral control volumes with cell widths Δx_i, Δy_j, Δz_k (non-uniform arrays). For each cell indexed by (i, j, k) we form the discrete energy balance by integrating Eq. (2) over the cell volume $V_{ijk} = \Delta x_i \Delta y_j \Delta z_k$.

For a face between cell p and neighbor q (across a coordinate direction), we compute the face conductance using the harmonic average of conductivities [11]:

$$k_{face} = \frac{2k_pk_q}{k_p+k_q} \quad (4)$$

The face conductance $G_{p\leftrightarrow q}$ used in the finite volume flux balance is the harmonic mean of adjacent conductivities [11]:

$$G_{p\leftrightarrow q} = \frac{k_{face}A_{face}}{d_{centers}} \quad (5)$$

where $d_{centers}$ is the center-to-center distance.

Summing fluxes and adding the complex mass term gives, for cell p [11]:

$$\sum_{q\in N_p}(-G_{p\leftrightarrow q})T_q + \left(\sum_{q\in N_p}G_{p\leftrightarrow q} + i\omega\rho c_pV_p\right)T_p = Q_pV_p + R_p \quad (6)$$

where Q_p is the volumetric heating rate (W m^{-3}) averaged in the cell, and R_p is any convective contribution moved to the right-hand side. Dividing by V_p gives the form used in the numerical calculation, where the off-diagonal coefficients are $-G/V_p$ and the diagonal stores the sum of the neighbor terms G/V_p plus $i\omega\rho c_p$.

Volumetric absorption in the fused silica with absorption coefficient μ_{sub} (m^{-1}) follows Beer–Lambert attenuation in depth.

In our calculations for gold particles, we use the miepython library [12]. Although Mie theory is formally derived for plane wave illumination, in this model the absorbed power is estimated by integrating plane wave absorption cross-sections weighted by the local Gaussian intensity profile, in the absence of significant multiple scattering. Mie theory yields the dimensionless efficiencies Q_{ext} (total extinction efficiency) and Q_{sca} (scattering efficiency), and thus the absorption efficiency [13]:

$$Q_{abs} = Q_{ext} - Q_{sca} \tag{7}$$

The absorption cross section is

$$\sigma_{abs} = Q_{abs}\pi R^2 \tag{8}$$

where R is the particle radius (m).

In the present model, particle absorption is incorporated through a volumetric absorption coefficient. The absorption cross section is converted into an equivalent volumetric absorption coefficient assigned to the computational cells overlapping the particle volume,

$$\alpha_{part} = \frac{0.75Q_{abs}}{R} \tag{9}$$

The focused Gaussian pump beam is propagated through the computational domain using a layer-by-layer Beer–Lambert attenuation. For each horizontal layer z_k, the local intensity is evaluated as

$$I(x, y, z_k) = I_0(x, y, z_k)exp\left[-\sum_{m=m_{surf}}^{k-1}\alpha(x, y, z_m)\Delta z_m\right] \tag{10}$$

where I_0 is the unattenuated Gaussian intensity profile and α(x,y,z) is the local volumetric absorption coefficient, including contributions from the substrate and from absorbing particles. The corresponding volumetric heat source is

$$q(x, y, z_k) = \alpha(x, y, z_k)I(x, y, z_k) \tag{11}$$

This approach accounts for mutual optical shadowing between multiple particles and for attenuation of the pump beam within the substrate, while remaining consistent with the absorption cross sections obtained from Mie theory. Within each particle, the absorbed energy is distributed uniformly over its volume through the constant coefficient α_{part}.

The present model assigns each particle a Mie absorption cross section. The layer-by-layer Beer–Lambert calculation accounts for sequential pump attenuation and optical shadowing, but it does not include electromagnetic multiple scattering or near-field coupling between particles. Consequently, the two particle results quantify thermal field overlap and signal broadening under the absorption approximation. Strongly optically coupled clusters would require a coupled electromagnetic solver to determine the absorbed power distribution and this is out of the scope in this work.

The thermal diffusion length for angular frequency ω is

$$\mu_{th}(\omega) = \sqrt{\frac{2a}{\omega}} \tag{12}$$

where μ_{th} characterizes the lateral/axial extent of the temperature oscillations and determines the thermal coupling between nearby defects.

The model computes the thermo-optic probe signal by converting the computed temperature field into an optical path change and then into a probe beam phase. The photothermal signal is calculated in a reflection mode (double-pass) configuration. The temperature is integrated along the probe beam path, and the refractive-index change is linearized using the thermo-optic coefficient dn/dT [14]:

$$\Delta l(x,y) = \int (n(T) - n_0)dz \approx \frac{dn}{dT}\int T(x,y,z)dz \quad (13)$$

The single-pass phase perturbation is

$$\Delta\varphi(x,y) = \frac{2\pi}{\lambda}\frac{dn}{dT}\int T(x,y,z)dz \quad (14)$$

Equation (14) defines the single-pass phase perturbation Δφ. In the reflection geometry used here, the probe enters at z = 0 and is assumed to reflect from an ideal planar interface at the rear boundary of the modeled substrate, z = 30 μm. It then retraces the same thermally perturbed path, so that the phase perturbation used in Eq. (15) is 2Δφ(x, y). The reflection coefficient and any reflector-induced phase shift are not modeled.

The simulator computes a probe-weighted average of Δφ to emulate finite-aperture probe detection:

$$S = \frac{\iint 2\Delta\varphi(x,y)W_2(x,y)dA}{\iint W_2(x,y)dA} \quad (15)$$

where W_2 is the probe Gaussian intensity profile. The modulus $|S|$ reflects the magnitude of the thermo-optical perturbation (the signal amplitude), while arg(S) represents the response-time delay caused by heat diffusion.

The linear system was solved using an incomplete-LU (ILU) preconditioned generalized minimal residual (GMRES) iterative solver [15].

Throughout this work, w_1 and w_2 denote the $1/e^2$ intensity radii of the Gaussian pump and probe beams, respectively. The standard values are w_1 = 2 μm and w_2 = 5 μm, corresponding to beam diameters of 4 and 10 μm. For the two-particle case with narrow pump beam, w_1 = 1 μm, corresponding to a 2 μm beam diameter. The gold particle radius is denoted separately by R = 2 μm (4 μm diameter)

3. Simulation

We performed simulations to study depth-resolved photothermal responses under the conditions summarized in Fig. 1. The parameters were λ_1 = 1064 nm, P_1 = 10 mW, and w_1 = 2 μm ($1/e^2$ intensity radius; 4 μm diameter) for the pump laser, and λ_2 = 633 nm, w_2 = 5 μm ($1/e^2$ intensity radius; 10 μm diameter) for the probe laser. The heating induced by the probe laser is neglected, as its absorbed power is assumed to be negligible compared with that of the pump beam. The domain size was 50 × 50 × 30 μm, and the particle radius was R = 2 μm (4 μm diameter). In all four cases, the defect is represented by a spherical gold particle embedded in a homogeneous fused-silica substrate. Parameters not mentioned here are listed in Table 1 and were identical for all cases, except case 4, where w_1 = 1 μm (2 μm diameter).

Table 1. Simulation parameters.

Parameter	Symbol	Value	Units
Domain size	$L_x \times L_y \times L_z$	50×50×30	μm
Thermal conductivity (substrate)	k_{sub}	1.38	W m^{-1} K^{-1}
Thermal conductivity (Au particle)	k_{Au}	318	W m^{-1} K^{-1}

Density, specific heat (Au)	ρ, c	19320, 129	kg m^{-3}; J kg^{-1} K^{-1}
Convection coeff. top (air)	h_{top}	20	W m^{-2} K^{-1}
Complex refractive index (Au)	n_{Au}	0.25846 + 6.9654i	—
Thermo-optic coefficient	dn/dT	1.2×10^{-5}	K^{-1}
Refractive index of fused silica	n_{sub}	1.453	—
Fused silica absorption coefficient	μ_{sub}	10^{-6}	cm^{-1}

The first (Fig. 1(a)) and second (Fig. 1(b)) cases were carried out to test whether the model reproduces the expected photothermal trends for defect depth, modulation frequency, and pump–probe focus alignment. The third and fourth cases were used to characterize the photothermal signal from subsurface defects for a single defect and for two closely spaced defects (Fig. 1(c) and 1(d)).

To provide a quantitative validation, we compared the finite-volume temperature amplitude with the harmonic point-source limit in an infinite homogeneous medium, $|T(r)| = P_{abs} \exp(-r/\mu_{th})/(4\pi kr)$, where $\mu_{th} = \sqrt{(2a/\omega)}$. At f = 1000 Hz, μ_{th} = 16.853 μm for the fused silica properties used here. For a single particle of radius R = 2 μm, the numerically integrated absorbed powers are 0.5274 and 0.7493 mW for pump beam focus positions of z = 0 and 8 μm, respectively. The point source expression is evaluated at r = R, i.e., at the particle surface.

The corresponding analytical estimates are 13.505 and 19.186 K, whereas the finite-volume maximum temperature amplitudes are 13.832 and 19.681 K, giving relative deviations of 2.42% and 2.58%. The Mie calculation gives Q_{abs} = 0.05555 and $\sigma_{abs} = 6.98 \times 10^{-13}$ m^2. This agreement supports the quantitative temperature scale of the model.

Figure 2(a) shows that all frequency traces exhibit a monotonic decrease in amplitude as the defect depth increases. A higher modulation frequency corresponds to a shorter thermal diffusion length [16]. Consequently, the highest amplitude at any given depth is observed at the lowest modulation frequency. The spacing between curves increases at shallow depths and collapses for deep defects, where diffusive attenuation dominates.

Figure 2(b) shows the phase of the complex photothermal signal measured at 1000 Hz as a function of defect depth. The plotted quantity is phase shift relative to the value at 4 μm. The observed behavior results from two principal complex contributions: a fixed surface contribution and a depth-dependent particle contribution.

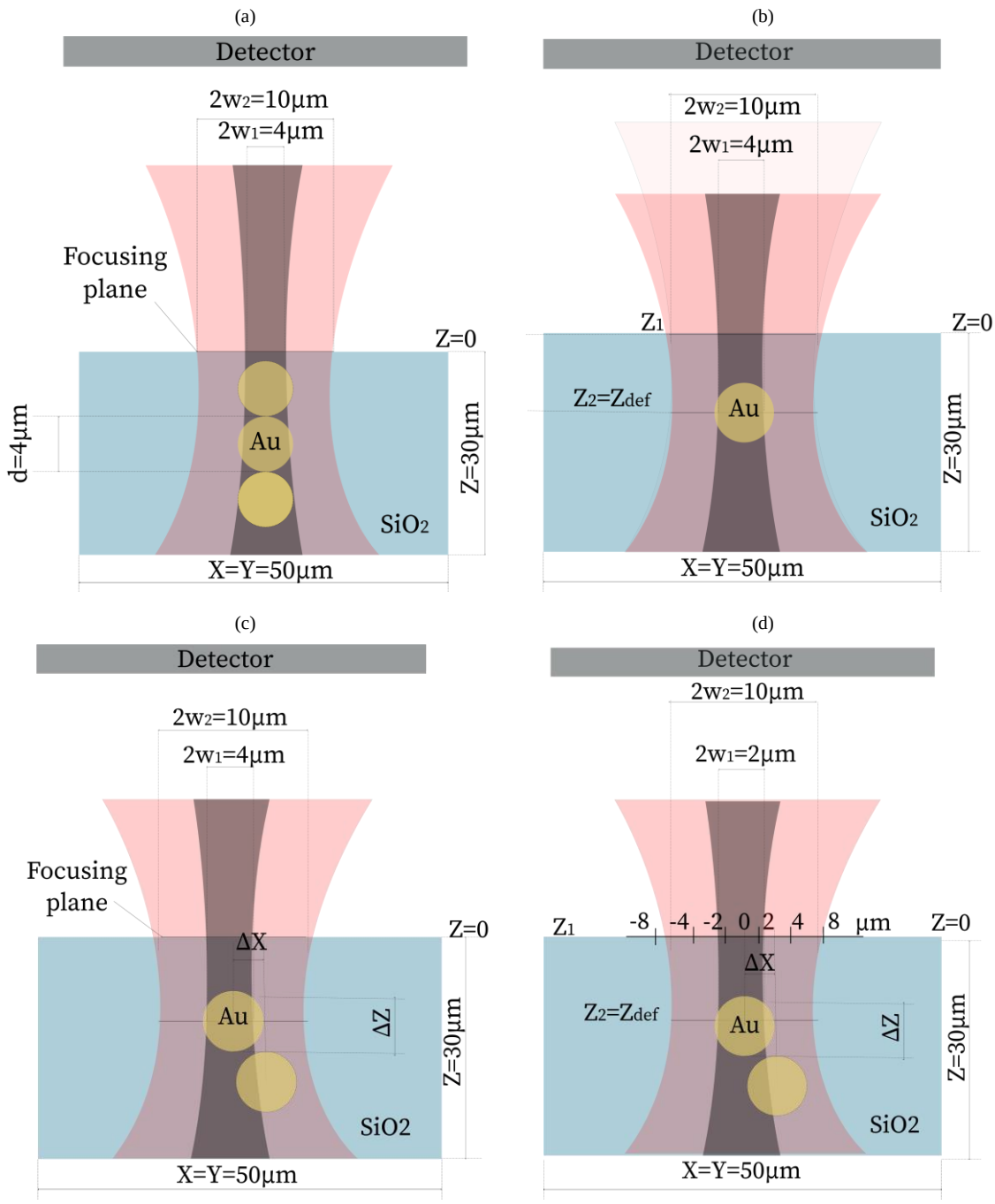
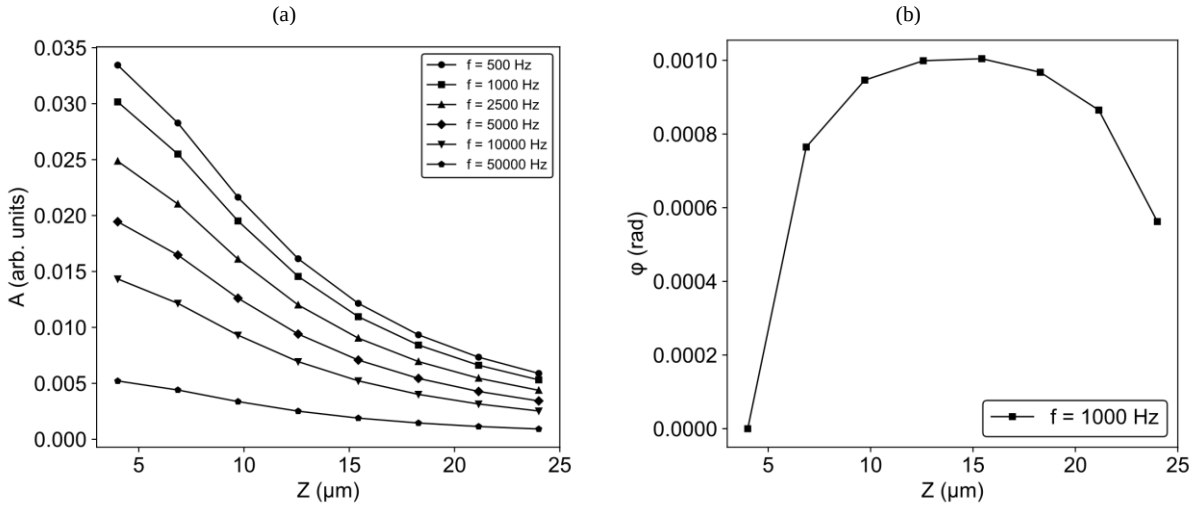


Fig. 1. (color online) Schematic of the cases solved using the finite volume method: determination of the photothermal signal dependence on (a) defect depth (defects are gold particles) by varying the depth in the positive Z-axis direction; (b) axial offset between the probe beam focal plane Z_1 and the pump beam focal plane Z_2, where $Z_2 = Z_{def}$ and Z_{def} is the defect depth; (c) defect depth for single and double defects; and (d) lateral (X-axis) scans for single and double defects with the pump beam focused at the substrate surface and at the defect-depth plane. The beam spreads from top to bottom.

The particle's complex response acquires an increasing phase lag with depth on the length scale set by thermal diffusion (for our substrate parameters this diffusion length is about 16 μm at 1000

Hz). At the same time, the particle amplitude varies with depth because of the pump laser intensity profile and the geometric overlap between pump laser, particle, and probe laser. As the defect depth increases from 4 to roughly 10 μm, the rotating particle phasor causes the total signal phasor to swing away from the surface reference, producing the rising normalized phase. For larger depths the particle contribution becomes too small to rotate the total phasor, and the observed phase returns toward the surface reference. The phase behavior is also consistent with photothermal single particle microscopy studies, where the measured phase delay is governed by finite thermal diffusivity around a heated gold particle [17].

For the case in Fig. 1(b), the defect is located at a depth of 8 μm. The relative signal amplitude in Fig. 2(c) refers to the normalized magnitude of the photothermal signal, expressed as the ratio of the signal amplitude at a given probe beam focal position to the amplitude when the probe focus is above the pump beam focus. As the probe beam focus moves deeper, the amplitude decays because the probe spatial weighting averages over regions with smaller ΔT. The map in Fig. 2(d) shows a pronounced ridge of maximum amplitude when the pump beam focus, probe beam focus, and the defect are co-located. Away from that ridge, the amplitude drops due to increased spatial mismatch [18]. The signal is strongly affected by optical geometry and by the relative positions of the pump beam, probe beam focus, and detection plane [19]. The maps also demonstrate that for a given pump–defect alignment there is a narrow band of probe focus depths that yield strong signals when the probe beam waist is small; as the probe waist increases, the high-signal band broadens but the peak sensitivity decreases.



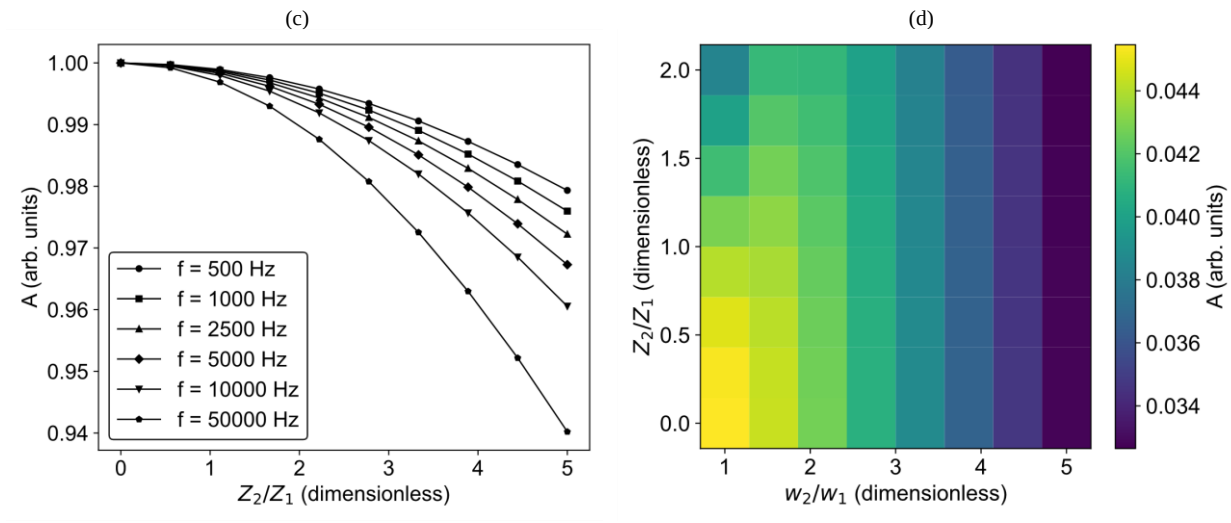


Fig. 2. (color online) (a) the dependence of the photothermal signal amplitude on the depth of the subsurface defect when both the pump and probe beams are focused at the top surface (Z = 0); (b) relative phase of the complex photothermal signal as a function of defect depth for the 1000 Hz frequency; (c) the relative photothermal signal amplitude as a function of the probe beam focal plane depth while the pump beam focus is fixed at the defect depth; (d) two-dimensional parameter maps.

Figure 3 presents lateral photothermal amplitude profiles obtained at a modulation frequency of 1000 Hz for single- and two-defect configurations under different pump beam focusing conditions. The lateral scan was performed along the X-axis from −8 μm to +8 μm, with a step size of 2 μm. A single central gold particle (radius 2 μm at a depth of 8 μm) is compared to a pair of identical particles, with the second particle positioned one particle diameter deeper along the Z-axis and shifted by one particle radius laterally along X. This arrangement represents clustered subsurface precursors in an optical substrate.

When the pump beam is focused at the substrate surface (Z = 0 μm), the single defect produces a clear central peak, while the two-defect case results in a broader profile with only slightly higher magnitude. This broadening arises from defocused heating, which illuminates a larger volume at the defect depth per scan step, increasing diffusive thermal spreading and overlap.

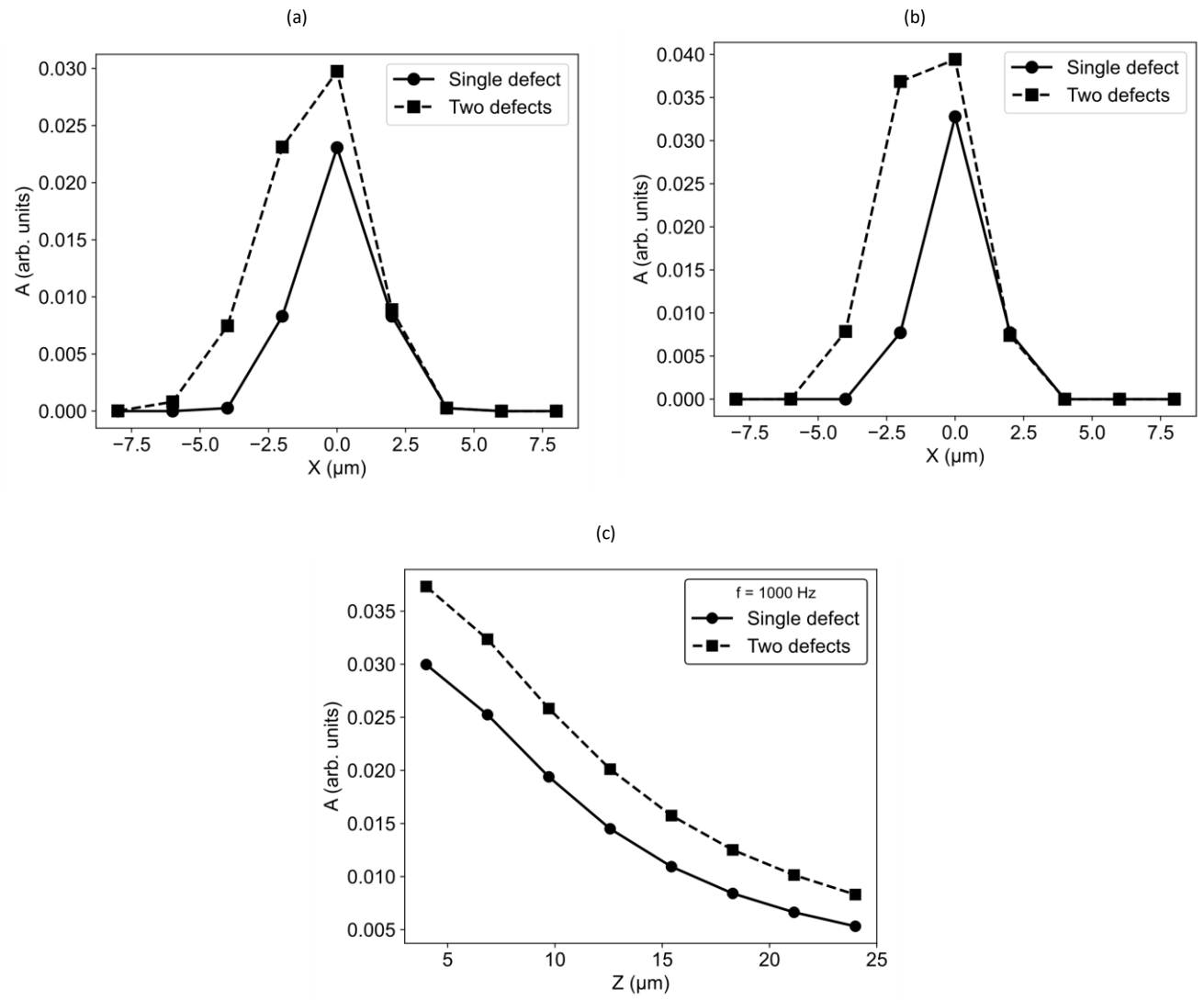


Fig. 3. (color online) The dependence of the photothermal signal amplitude for the cases of one and two defects: (a) pump beam focusing plane Z = 0 μm, w_1 = 2 μm; (b) pump beam focusing plane Z = 8 μm, w_1 = 2 μm; (c) the dependence of the photothermal signal amplitude on the depth of the two subsurface defects. Modulation frequency 1000 Hz.

In contrast, focusing the pump beam at the defect plane (Z = 8 μm) yields higher amplitudes for both the single- and two-defect cases, with the double defects exhibiting a more pronounced and confined response. For the two 1D scanning scenarios considered (2D mapping is beyond the scope of this work), one can see that the amplitude profiles for the two-defect case can often be misinterpreted as originating from a single larger defect. This underscores the necessity, in experiment, of performing scans in multiple cross-sections to correctly resolve defect multiplicity and geometry. Time-harmonic heating theory for plasmonic particles also predicts modulation frequency dependent amplitude and phase responses and describes thermal coupling in multiple particle systems [9].

Figure 4 complements these results by visualizing the simulated steady-state temperature amplitude distribution resulting from modulated heating of the two closely spaced gold particles, illustrating the thermal overlap between the particles. Temperature magnitudes are consistently higher when the pump is focused at the defect plane, reflecting more localized energy deposition and reduced diffusive losses, in agreement with the enhanced signals observed in Fig. 3.

These results indicate that the finite volume method can capture the features of the photothermal signal amplitude during 1D lateral scanning for different pump waist sizes and the three-dimensional temperature distribution within the defects and substrate simultaneously. The model's flexibility allows extension to defects of arbitrary shapes and morphologies.

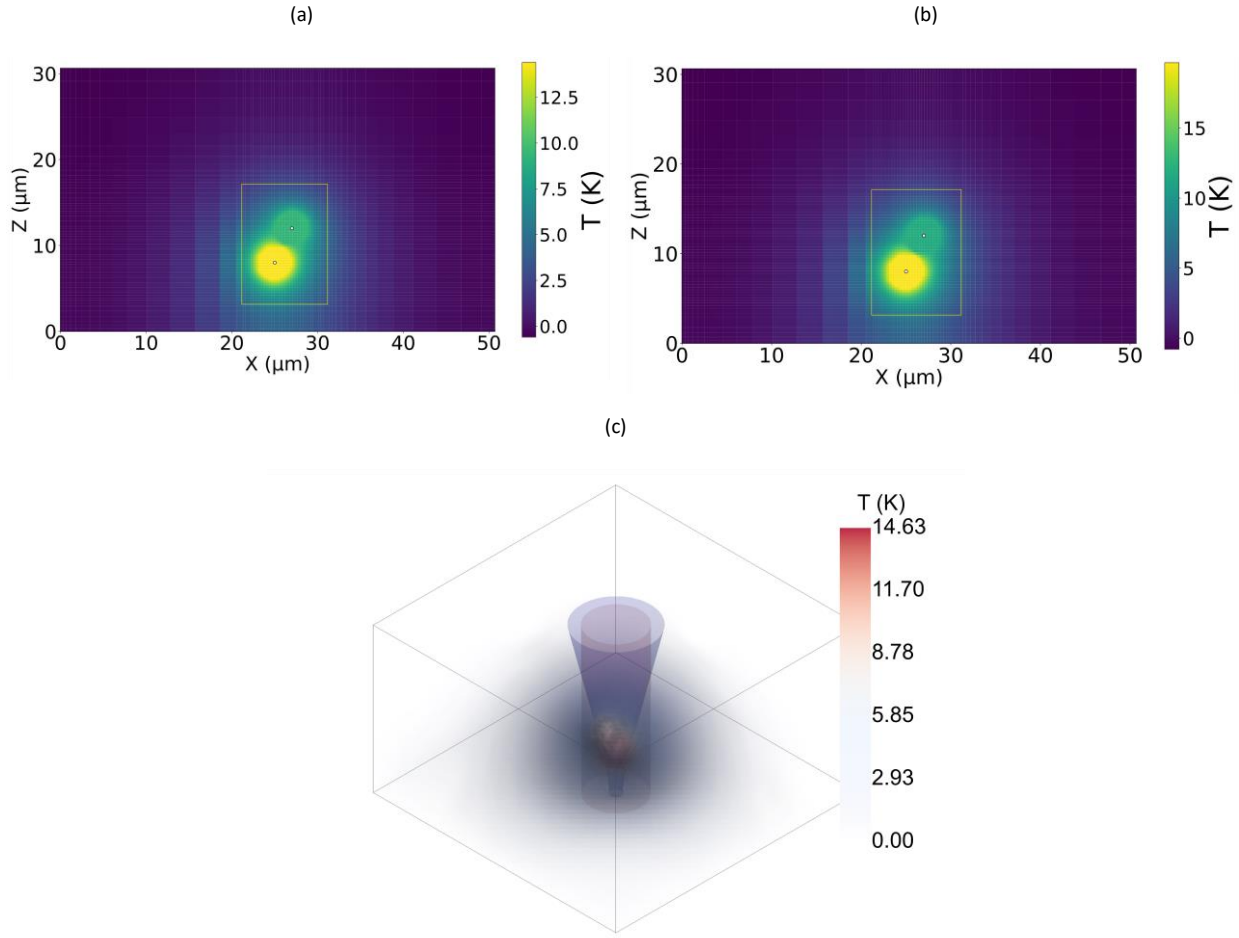


Fig. 4. (color online) Temperature distribution of two gold particles and the substrate in the (a) XZ cross-section for the pump beam focusing plane at Z = 0 μm, w_1 = 2 μm; (b) XZ cross-section for the pump beam focusing plane at Z = 8 μm, w_1 = 2 μm; (c) 3D view for the pump beam focusing plane at Z = 0 μm, w_1 = 2 μm. The pump beam profile used for 3D visualization is shown in blue and the probe beam profile in red. The beams spread from bottom to top.

4. Conclusion

We have developed and tested a frequency domain finite volume numerical model for photothermal microscopy that computes probe beam weighted thermo-optical responses of subsurface absorbing particles. The implementation couples Mie theory particle absorption estimates to a volumetric heat source, solves the harmonic heat equation on an adaptive non-uniform 3D grid, and obtains the steady-state complex temperature field via an ILU-preconditioned GMRES solver. The simulated optical signal is obtained by integrating the temperature induced refractive index change along the optical axis and averaging it with the probe intensity profile; the resulting complex scalar yields amplitude and phase metrics.

Numerical experiments reproduce the principal physical trends expected for diffusive heat transport: the photothermal amplitude decays with increasing defect depth and with increasing modulation frequency, while the measured phase exhibits an increase up to a certain defect depth. Parameter maps of pump/probe focus depth and beam waists identify narrow regions of maximal sensitivity where the pump and probe overlap the defect; these maps quantify focus and beam size tolerance. Two-particle simulations demonstrate that closely spaced absorbers generate thermal overlap that produces non-additive amplitude responses, indicating the need to consider thermal overlap when interpreting experimental signals. The two-particle calculations use Mie absorption cross sections and Beer–Lambert attenuation. Electromagnetic multiple scattering and near-field coupling are not included. The reported broadening therefore quantifies thermal field overlap under the absorption approximation.

A particular strength of the finite volume approach on adaptive nonuniform grids is its flexibility to analyze defects of arbitrary shapes, sizes, and distributions (e.g., voids, cracks, or irregular inclusions). This allows direct visualization of three-dimensional temperature fields and the resulting photothermal signals for diverse defect morphologies. The present model provides a numerical foundation for further development, in which additional optical and thermal effects can be incorporated as required. It also establishes a basis for direct comparison with future measurements on calibration substrates containing intentionally embedded gold particles, enabling the model assumptions and parameters to be refined. Experimental validation therefore represents a natural next stage of this work.

Data availability statement: The data that support the findings of this study are available from the corresponding author upon reasonable request.

Acknowledgment: Project supported by the CAS-ANSO Scholarship (Grant No. 2024ANP00117).

References

[1] Bertussi B, Natoli J Y and Commandré M 2006 *Appl. Opt.* **45** 1410
[2] Adhikari S, Spaeth P, Kar A, Baaske M D, Khatua S and Orrit M 2020 *ACS Nano* **14** 16414
[3] Wang Y, Wang F, Song P and Liu J 2023 *Opt. Lett.* **48** 1750
[4] Shi Z, Sun L, Shao T, Liu H, Huang J, Ye X, Wang F, Yang L and Zheng W 2022 *Photonics* **9** 137

[5] Zhang X and Li B 2015 *Rev. Sci. Instrum.* **86** 024902
[6] Zhang X and Li B 2018 Rev. Sci. Instrum. **89** 024901
[7] Chirtoc M and Horny N 2022 *J. Appl. Phys.* **131** 214502
[8] Blum O and Shaked N T 2015 *Light Sci. Appl.* **4** e322
[9] Berto P, Mohamed M S A, Rigneault H and Baffou G 2014 *Phys. Rev.* B **90** 035439
[10] Mandelis A 2001 *Diffusion-Wave Fields* (New York: Springer)
[11] Patankar S V 2018 *Numerical Heat Transfer and Fluid Flow* (1st edn.) (Boca Raton: CRC Press)
[12] Prahl S 2025 *miepython: Pure Python Calculation of Mie Scattering* (Zenodo) https://doi.org/10.5281/zenodo.7949263
[13] Bohren C F and Huffman D R 1998 *Absorption and Scattering of Light by Small Particles* (New York: Wiley)
[14] Whinnery J R 1974 *Acc. Chem. Res.* **7** 225
[15] Saad Y and Schultz M H 1986 *SIAM J. Sci. Stat. Comput.* **7** 856
[16] Jackson W B, Amer N M, Boccara A C and Fournier D 1981 *Appl. Opt.* **20** 1333
[17] Heber A, Selmke M and Cichos F 2015 *Phys. Chem. Chem. Phys.* **17** 20868
[18] Swofford R L and Morrell J A 1978 *J. Appl. Phys.* **49** 3667
[19] Bialkowski S E and Chartier A 1997 *Appl. Opt.* **36** 6711